Geophysical Journal International

Geophys. J. Int. (2012) **190,** 1593–1606 doi: 10.1111/j.1365-246X.2012.05564.x

Theory and feasibility tests for a seismic scanning tunnelling macroscope

Gerard T. Schuster,[1] Sherif Hanafy[1,2] and Yunsong Huang[1]

[1] *King Abdullah University of Science and Technology (KAUST), PSE Division, Thuwal* 23955-6900*, Saudi Arabia. E-mail: gerard.schuster@kaust.edu.sa*
[2] *Geophysics Department, Faculty of Science, Cairo University, Giza, Egypt*

Accepted 2012 June 1. Received 2012 June 1; in original form 2011 July 7

SUMMARY

We propose a seismic scanning tunnelling macroscope (SSTM) that can detect subwavelength scatterers in the near-field of either the source or the receivers. Analytic formulas for the time reverse mirror (TRM) profile associated with a single scatterer model show that the spatial resolution limit to be, unlike the Abbe limit of $\lambda/2$, independent of wavelength and linearly proportional to the source-scatterer separation as long as the scatterer is in the near-field region. This means that, as the scatterer approaches the source, imaging of the scatterer with super-resolution can be achieved. Acoustic and elastic simulations support this concept, and a seismic experiment in an Arizona tunnel shows a TRM profile with super-resolution adjacent to the fault location. The SSTM is analogous to the optical scanning tunnelling microscopes having subwavelength resolution. Scaled to seismic frequencies, it is theoretically possible to extract 100 Hz information from 20 Hz data by the imaging of near-field seismic energy.

Key words: Interferometry; Theoretical seismology; Wave scattering and diffraction; Wave propagation.

INTRODUCTION

The resolution limit in refocusing light waves by a conventional optical lens is defined as the Rayleigh resolution limit (Elmore & Heald 1969; Born & Wolf 1999) $\Delta\theta = 1.22\lambda/D$, or if the object is close enough to the lens such as in a microscope then there is the Abbe resolution limit. Here, $\Delta\theta$ is the angle between the optic axis and the line that connects the object in the image plane with the edge of the lens, D is the aperture width of the circular optical lens and λ is the wavelength associated with the light. This resolution limit is important for defining the minimum distance between two neighbouring objects in which they are distinguishable in the image.

To achieve better resolution than the Abbe limit, evanescent energy should be used for imaging. In 1873, Abbe recognized a fundamental diffraction limit of optics: whenever an object is imaged by an optical lens, fine features of the object smaller than $\lambda/2$ are permanently lost in the image (Cragg & So 2000; Zhang & Liu 2008). Such fine detailed information is lost because light emerging with these fine features decays exponentially away from the object as evanescent energy, and are not carried by the propagating waves (Tabib-Azar *et al.* 1999; de Rosny & Fink 2002; Lerosey *et al.* 2007; Fink 2008). If this subwavelength information can be utilized then there is the possibility of subwavelength imaging, also known as super-resolution (Steel *et al.* 2010), and forms the basis of many types of high-resolution optical imaging devices (de Fornel 2001; Jia *et al.* 2010). Until now, such a device has not been devised for seismic waves in the earth.

Resolution that goes beyond Rayleigh resolution without using near-field evanescent energy in seismic imaging can be achieved by applying various algorithms to the data, such as diffraction tomography (Schatzberg & Devaney 1992; Gelius 1995), least squares migration (Nemeth *et al.* 1999; Duquet *et al.* 2000; Kuhl & Sacchi 2003), conventional statistical multiple signal classification (Schmidt 1986; Lehman & Devaney 2003), or null space solutions (Gelius & Asgedom 2011). An overview of diffraction-limited resolution for seismic applications is provided by Gelius & Asgedom (2011).

This article shows both theoretically and experimentally that it is possible to use far-field seismic energy for subwavelength imaging of sources at seismic frequencies. The key idea is that seismic energy scattered from subwavelength objects located in the near-field of the source or receiver can be refocused with subwavelength resolution by TRMs to the source location. This is similar to optical imaging devices that include a super lens in the near field of the source (i.e. within a half-wavelength distance) that converts the evanescent energy to propagating waves (de Fornel 2001). Analogous to the STM (de Fornel 2001) we propose a seismic scanning tunnelling macroscope (SSTM) that can harness the subwavelength imaging potential in near-field seismic energy.

This paper is organized in the following way. The first section presents the SSTM theory and shows how its essential properties are related to the point scatterer response of the near-field TRM operator. A related formula is derived in Appendix B that shows the influence of second-order scattering from multiple scatterers. The second section presents acoustic simulations that validate predictions from the SSTM theory for multiple scatterers. This is followed by the next section which presents elastic simulations of TRM profiles and field data results from a seismic experiment in an Arizona

tunnel. The elastic simulations suggest that the acoustic theory is largely valid for an elastic medium and are consistent with the field data results. The last section presents the conclusions.

SEISMIC SCANNING TUNNELLING MACROSCOPE

The SSTM shares the same principle as the scanning tunnelling microscope (STM) in producing images with high spatial resolution: small near-field changes in the separation of the source-object lead to enormous changes in the measured field. In the case of the STM, the measured field is the current at the scanning tip and for the SSTM it is the amplitude changes in the scattered field.

Fig. 1(a) illustrates this idea for the STM (Binnig & Rohrer 1986; Bai 2000) where a conducting tip (a few atoms in width) is placed within a few Angstroms from the conducting surface of the object. The goal is to map out the topography of the conducting surface to within a few Angstroms of resolution. If the object is within the near-field of the tip, electrons can tunnel through the vacuum gap to create a current between the tip and object. This near-field current measured at the tip is very sensitive to slight changes in the height of the surface, as illustrated by the $I(h)$ versus h plot on the right. Consequently, scanning the tip just above the surface (i.e., in the near-field region of the object's surface) can map out the surface topography to within a few nanometres. If the tip is too far away from the surface, that is, it is in the far-field region, then current fluctuations due to topography variations are too weak to be reliably measured. Analogously, the SSTM illustrated in Fig. 1(b) relies on the fact that the scattered seismic energy from a subwavelength scatterer is very sensitive to the changes in the near-field separation r between the source and scatterer. This strong sensitivity is caused by the strong sensitivity of the geometric spreading term $1/r$ to small near-field variations in the source-scatterer separation r (see A(h) versus h curve in Fig. 1(b), where r and h are the same). Note, the evanescent wave from the source converts to a propagating body wave at the scatterer that is recorded by the receivers, also illustrated in Fig. 2. Unlike the STM, the SSTM receivers are in the far-field region of the source and the recorded seismic energy is refocused to

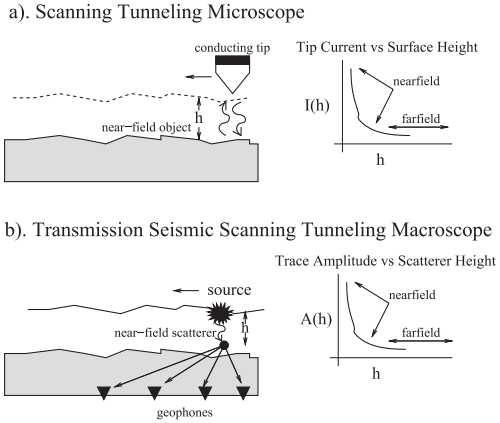

Figure 1. Illustration of (a) Scanning Tunnelling Microscope (STM) and (b) Seismic Scanning Tunnelling Macroscope in transmission mode. In the STM (SSTM) example, small changes in the source-object (source-scatterer) separation lead to enormous changes in the measured current (trace amplitude of scattered energy) measured at the tip (geophone). It is assumed that both the tip (seismic source) and object (seismic scatterer) are subwavelength in dimension and are separated by less than $\lambda/2$.

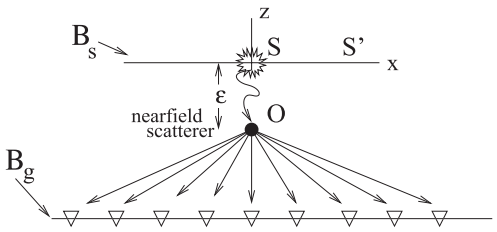

Figure 2. Single scatterer in the near field of the source and the geophones are in the far-field region. The horizontal resolution limit of the source image is proportional to ϵ for a homogeneous background medium.

the source position by a TRM operation. The next section presents the mathematical formulation for refocusing waves by the TRM.

Point scatterer response of the near-field TRM operator

To understand the properties of refocusing seismic waves by TRMs we first derive its point scatterer response function. This function, similar to the point spread function (Lipson *et al.* 1995) used in optical physics and seismic migration (French 1974), is a valuable diagnostic tool for understanding the focusing sensitivity to variations in the object distance, the recording geometry and the wavelength.

In Fig. 2, the point scatters at $\mathbf{o} = (0, \epsilon)$ scatters incoming energy from the harmonic point source at $\mathbf{s} = (0, 0)$, which is then recorded by receivers at $\mathbf{g}\epsilon B_g$. The scattered data $G(\mathbf{g}|\mathbf{s})^{\text{scatt.}}$ can be mathematically expressed as

$$\mathbf{s}\epsilon B_s;\ \mathbf{g}\epsilon B_g; \quad G(\mathbf{g}|\mathbf{s})^{\text{scatt.}} = G(\mathbf{g}|\mathbf{o})G(\mathbf{o}|\mathbf{s}), \tag{1}$$

where a unity scattering coefficient is conveniently assumed and $G(\mathbf{x}|\mathbf{x}')$ is the Green's function that solves the Helmholtz equation for a point source at $\mathbf{x}'$ and a receiver at $\mathbf{x}$ in a background velocity model. The dependence on the angular frequency variable ω is implicit in this Green's function notation. For a band-limited point source at $\mathbf{s}$ with wavelet spectrum $W(\omega)$, the TRM image $m(\mathbf{s}', \mathbf{s})$ with a trial point source at $\mathbf{s}'\epsilon B_s$ for a continuous distribution of geophones along B_g is given by

$$\mathbf{s}'\epsilon B_s; \quad m(\mathbf{s}', \mathbf{s}) = \int_{-\omega_0}^{\omega_0}\int_{-L}^{L} k|W(\omega)|^2 \overbrace{G(\mathbf{g}|\mathbf{o})G(\mathbf{o}|\mathbf{s})}^{\text{scattered data}}\overbrace{G(\mathbf{g}|\mathbf{o})^* G(\mathbf{o}|\mathbf{s}')^*}^{\text{extrapolator}} \mathrm{d}\mathbf{g}\mathrm{d}\omega. \tag{2}$$

If the background medium is homogeneous with velocity c, the background Green's function is

$$G(\mathbf{x}|\mathbf{x}') = \frac{e^{i\omega|\mathbf{x}-\mathbf{x}'|/c}}{|\mathbf{x}-\mathbf{x}'|}, \tag{3}$$

where $k = \omega/c$, the frequency band of the flat source spectrum is between $-\omega_0$ and ω_0, and the recording aperture is $2L$ wide. The extrapolator plays the role of focusing the recorded energy back to the source location. If the source is the reflection point at a reflector boundary, then the related imaging is called reverse time migration (McMechan 1983; Claerbout 1992) for extrapolators computed by finite-difference solutions to the wave equation; and if a Kirchhoff-like formula is used to extrapolate poststack traces it is called poststack migration (French 1974; Schuster 2009). If the data are used for the extrapolator then eq. (2) forms the basis of the operation known as the time reverse mirror (TRM; Fink 1993, 2006, 2008). It is now known that the general mathematical foundation for these methods is the reciprocity theorem of correlation type (Snieder 2004; Wapenaar 2004).

For convenience, assume $|W(\omega)|^2 = 1/k$ so that plugging the Green's function in eq. (3) into eq. (2) gives the TRM profile $m(\mathbf{s}', \mathbf{s})$

$$m(\mathbf{s}', \mathbf{s}) = \int_{-\omega_0}^{\omega_0} \frac{e^{\mathrm{i}\omega(|\mathbf{o}-\mathbf{s}|-|\mathbf{o}-\mathbf{s}'|)/c}}{|\mathbf{s}-\mathbf{o}||\mathbf{s}'-\mathbf{o}|}\mathrm{d}\omega \int_{-L}^{L} \frac{1}{|\mathbf{g}-\mathbf{o}|^2}\mathrm{d}g,$$
$$= \frac{\alpha(\mathbf{s}, \mathbf{o}, \mathbf{s}')\sin(\omega_0[|\mathbf{o}-\mathbf{s}| - |\mathbf{o}-\mathbf{s}'|]/c)}{[|\mathbf{o}-\mathbf{s}| - |\mathbf{o}-\mathbf{s}'|]}, \quad (4)$$

where the near-field geometrical spreading factor $\alpha(\mathbf{s}, \mathbf{o}, \mathbf{s}')$ is defined as

$$\alpha(\mathbf{s}, \mathbf{o}, \mathbf{s}') = \frac{c}{|\mathbf{s}-\mathbf{o}||\mathbf{s}'-\mathbf{o}|}\int_{-L}^{L} \frac{1}{|\mathbf{g}-\mathbf{o}|^2}\mathrm{d}g. \quad (5)$$

Eq. (4) is used to compute the TRM profile for the trial source positions $\mathbf{s}'$ along a specified line that intersects the actual source position.

For a fixed source position $\mathbf{s}$, the first zero-crossing of $m(\mathbf{s}', \mathbf{s})$ is given by the value of $\mathbf{s}'$ that satisfies

$$[|\mathbf{o}-\mathbf{s}| - |\mathbf{o}-\mathbf{s}'|] = -\lambda_0/2, \quad (6)$$

and, under the traditional Rayleigh resolution criterion, determines the spatial resolution of the imaged source location; here $\lambda_0 = 2\pi c/\omega_0$. For the scatterer at $\mathbf{o} = (0, \epsilon)$, the source at $\mathbf{s} = (0, 0)$, and $\mathbf{s}' = (x', 0)$, eq. (6) becomes

$$\left[\epsilon - \sqrt{\epsilon^2 + x'^2}\right] = -\lambda_0/2. \quad (7)$$

For $\epsilon \approx 0$ the first zero-crossing is at $x' = \lambda_0/2$, which is the Abbe limit and the sinc-like function is illustrated by the solid-line curves in Fig. 3. As expected, the sinc-like function widens as the point scatterer is moved further away from the point source.

However, the first zero-crossing is not the only determinant of the spatial resolution limit Δx because the near-field geometrical spreading factor $\alpha(\mathbf{s}, \mathbf{o}, \mathbf{s}')$ in eq. (5) is proportional to $\frac{1}{|\mathbf{s}'-\mathbf{o}|}$, which spikes the central part of the sinc function for small ϵ. This spiking is illustrated by the dashed-line curves in Fig. 3, where the half-width of $\frac{1}{|\mathbf{s}'-\mathbf{o}|}$ is shown in Appendix A to be

$$\Delta x' = \beta\epsilon. \quad (8)$$

Consequently, the near-field horizontal resolution becomes better as the point scatterer approaches the source position. Here, β is a constant that depends on the type of resolution criterion and is equal to $2\sqrt{3}$ if a half-power criterion is used. In the Fig. 3 example, the dominant wavelength of the transient source is 120 m. Beyond the source-scatterer distance of about $\lambda/2$ the sinc-like function determines the horizontal resolution limit, otherwise it is controlled by the inverse-distance function to yield subwavelength resolution.

Eq. (8) says that the evanescent energy introduces an effective horizontal wavelength that is linearly proportional to the distance between the point scatterer and the point source. And for source-scatterer separations greater than $\lambda/2$ the sinc-like function controls lateral resolution, not the near-field geometrical spreading factor in eq. (5).

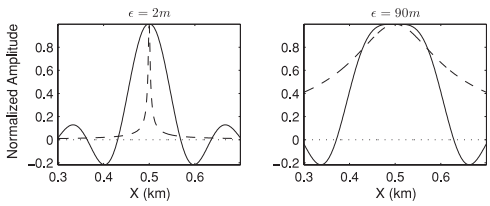

Figure 3. Plots of sinc-like function (solid lines) in eq. (4) and inverse-distance function (dashed lines) in eq. (5) for a point scatterer 2 m (left plot) and 90 m (right plot) from the point source.

SUBWAVELENGTH SCATTERERS WITH FINITE VOLUME

The TRM profile of a point scatterer showed that rapid near-field variations of the geometrical spreading term accounted for superresolution in the TRM profile. This is also true for subwavelength scatterers with finite volume. To prove this, Godin (2011) derives the acoustic response p_{sc} for the near-field scattering from a soft sphere of radius a due to a near-field point source:

$$p_{sc} = -\frac{a}{b}\left[\frac{e^{\mathrm{i}kR}}{R} + \mathrm{i}k(b-a)\frac{e^{\mathrm{i}kr}}{r}\right]$$
$$\times [1 + O(k^2(b^2 + r^2))], \quad (9)$$

where $b > a$ is the radius of a reference sphere larger than the scatterer's radius; and r (R) represents the distance between the near-field observation point and the centre of an image point within the sphere. Similar to the Green's function for a point scatterer, the near-field scattering of a small sphere has an inverse distance sensitivity to slight changes in the observation location[1].

For a point scatterer, the entire domain $h > 0$ of $A(h)$ in Fig. 1 is available for superresolution profiling and so the TRM profile has a potentially unlimited resolution capability according to eq. (8). In contrast, scattered data from a spherical scatterer of radius a only gives access to the domain $h > a$, and so $\epsilon > a$ in eq. (8).

Finally, a subwavelength scatterer does not have to be spherical to promote superresolution. For example, the asymptotic near-field Green's function for a wedge (Osipov & Hongo 1998) is inversely proportional to the square root of distance from the wedge.

ACOUSTIC SIMULATION TESTS

Synthetic acoustic data are now used to test for subwavelength resolution, where a Born modelling procedure with ray tracing generates the scattered data (Stolt & Benson 1986). For multiple scatterers with weak interactions, the Born formula is used to compute the scattered pressure field $d(\mathbf{g}, t|\mathbf{s}, 0)^{\text{scatt.}}$ due to a point source at $\mathbf{s}$ excited at time zero and recorded at $\mathbf{g}$

$$d(\mathbf{g}, t|\mathbf{s}, 0)^{\text{scatt.}} =$$
$$\mathcal{F}^{-1}\left[W(\omega)\sum_{\mathbf{o}\epsilon B_o}\frac{r(\mathbf{o})e^{\mathrm{i}k(|\mathbf{g}-\mathbf{o}|+|\mathbf{o}-\mathbf{s}|)}}{|\mathbf{g}-\mathbf{o}||\mathbf{o}-\mathbf{s}|}\right], \quad (10)$$

where $W(\omega)$ is the spectrum of a Ricker source wavelet, $\mathcal{F}^{-1}$ represents the inverse Fourier temporal transform, and $r(\mathbf{o})$ is the scattering coefficient associated with the point scatterer at $\mathbf{o}\epsilon B_o$. Here, B_o is the set of point scatterer locations. For multiple scatterers in a homogeneous medium, the modelling formula is highly accurate if second-order and higher-order multiples are negligible. If the multiples are stronger, then the scatterer–scatterer reverberations can possibly enhance the effectiveness of the SSTM in detecting small-scale scatterers.

[1] Note, the asymptotic limit $k^2(b^2 + r^2) \to 0$ as the radius of the scatterer becomes small with respect to the wavelength.

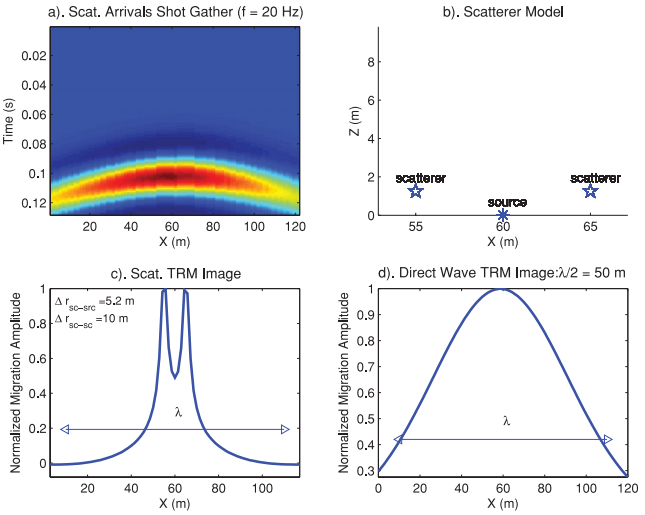

Figure 4. (a) Shot gather for the two-scatterer model in (b) where the point source is at $(x, z) = (60, 0)$ m; here, the source time history is that of a Ricker wavelet peaked at 20 Hz and the horizontal line of geophones is 45 m above the source. The scatterers are located in the near-field region of the source (5.2 m source-scatterer separation), where the wavelength of the source is 100 m. (c) The TRM profile at $z = 0$ for a source at $\mathbf{s} = (60, 0)$ m using only scattered arrivals shows a horizontal resolution of approximately $\lambda/20$; here the horizontal axis indicates the trial source position $\mathbf{s}'$ in eq. (11). In contrast, the TRM profile using only the direct arrivals is in (d) and shows diffraction-limited resolution.

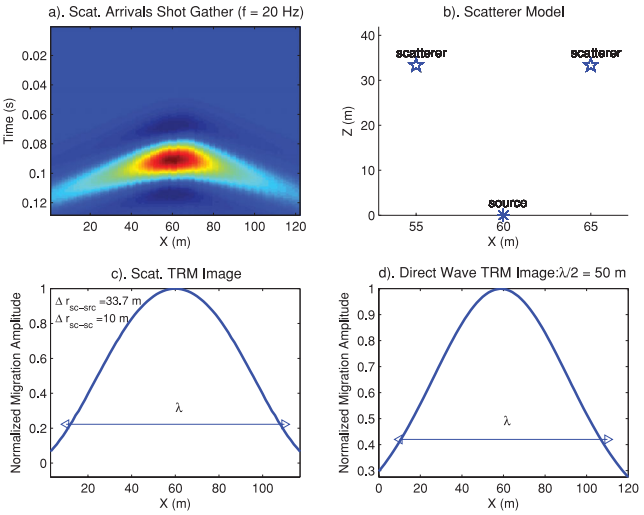

Figure 5. Same as Fig. 4, except the scatterer-source separation is 33.7 m rather than 5.2 m. Here, super-resolution profiling is lost in c) because the scatterers are more than 1/3 of a wavelength from the source.

For multiple point scatterers embedded in a homogeneous background model, the TRM imaging formula 2 becomes

$$\mathbf{s}'\epsilon B_s;\;\; m(\mathbf{s}', \mathbf{s}) = \int_{-\omega_0}^{\omega_0} k|W(\omega)|^2 \times \overbrace{\sum_{B_g}\sum_{\mathbf{o}\epsilon B_o} r(\mathbf{o})G(\mathbf{g}|\mathbf{o})G(\mathbf{o}|\mathbf{s})}^{\text{scattered data}} \times \overbrace{\sum_{\mathbf{o}'\epsilon B_o} r(\mathbf{o}')G(\mathbf{g}|\mathbf{o}')^* G(\mathbf{o}'|\mathbf{s}')^*}^{\text{extrapolator}} \mathrm{d}\omega, \tag{11}$$

where the summations are over the scatterer locations in the set B_o and the geophone locations in B_g. In this formula, the input scattered data consist of the scattered energy recorded at $\mathbf{g}\epsilon B_g$ excited by a single source at $\mathbf{s}\epsilon B_s$, and the output of this equation is the TRM profile $m(\mathbf{s}', \mathbf{s})$ for different trial image points $\mathbf{s}' = (x, 0.5)\epsilon B_s$ as depicted in Figs 4(c)–(d).

Subwavelength resolution for acoustic data

Fig. 4(a) depicts 85 traces in a shot gather for the two scatterer model in Fig. 4(b) with a source at (60, 0) m; only the scattered arrivals are computed here. These traces were computed with eq. (10), where the scatterers are separated by 10 m and located 5.2 m from the source (60, 0) m. Here, the source time history is that of a Ricker wavelet peaked at 20 Hz and the horizontal line of geophones is 45 m above the source. The traces are used as input to eq. (11) to create the TRM profile in Fig. 4(c). It is obvious that this TRM profile clearly distinguishes the separation of the two scatterers from one another, despite the 100 m wavelength. The horizontal resolution of this scattered wave TRM profile is approximately $\lambda/20$. In contrast,

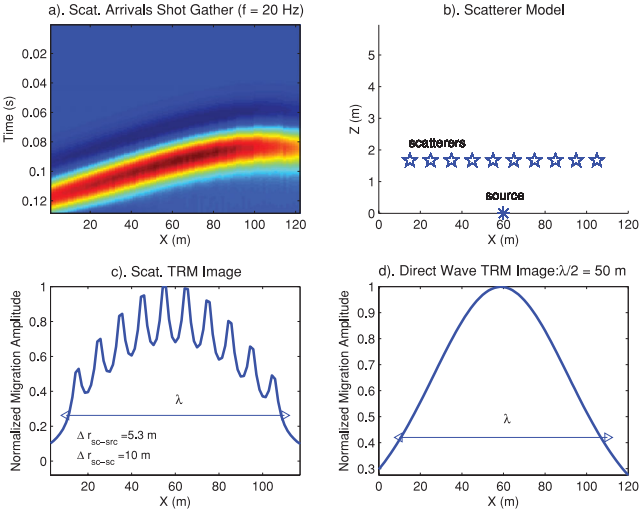

Figure 6. Same as Fig. 4, except there are 10 scatterers with the same reflection coefficient, each separated by 5.2 m. Here, super-resolution profiling is achieved at far offset positions (e.g. $X = 20$ m) from the source. See Appendix B for an explanation.

the TRM profile associated with the direct wave in Fig. 4(d) is diffraction limited.

If the two scatterers are elevated to 33 m (about 1/3 the wavelength separation) above the source line with a source at (60, 0) m, then the resulting TRM profile loses its super-resolution property, as depicted in Fig. 5. According to theory (see Fig. 3), moving the scatterers out of the near-field region and into the far-field prevents the utilization of the evanescent energy in resolving model details.

Fig. 6(a) depicts the shot gather for a source located at $(x, z) = (120, 0)$ m on the bottom right of the 10-scatterer model in Fig. 6(b). The corresponding TRM profile in Fig. 6(c) for a point source at (60, 0) m shows that subwavelength resolution is possible for many scatterers near the source line, as explained in Appendix B. In fact, the location of the scatterers projected onto the receiver line approximately coincides with the horns in the TRM image. As the scatterer line is moved away from the source line, the scatterers will no longer be in the source's near-field region and so the spiky horns

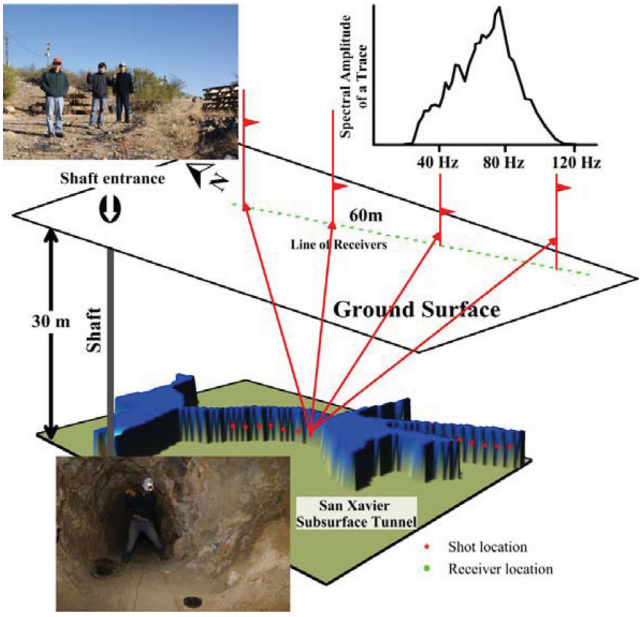

Figure 7. Sketch of source–receiver geometry and tunnel for seismic experiment near Tucson, Arizona. The line of sources in the subsurface mine (upper level) is roughly parallel to the receiver line shown at the surface. The power spectrum of a typical trace is shown in the upper right diagram.

will smooth out to the shape of a Gaussian-like curve. These results suggest that a downhole source can possibly be used to scan along the source well and use the TRM profile to qualitatively reveal, at subwavelength resolution, the character of near-field scatterers. This defines the SSTM procedure.

ELASTIC SIMULATION AND TUCSON FIELD DATA TESTS

The SSTM is now tested with both elastic simulations and seismograms recorded at a seismic experiment in an Arizona tunnel. A finite-difference solution to the 2-D elastic wave equation is used to generate the elastic seismograms, which are then used to get the TRM profiles. The field data test is a controlled-source seismic experiment[2] conducted at the San Xavier Mining Lab, near Tucson, Arizona where the source is a hammer blow in a subsurface mine. The resulting vibrations are recorded along a horizontal line of vertical-component receivers located about 30 m above the source line in Fig. 7. The goal is to detect in the TRM profile super-resolution associated with scatterers in the near-field of the source.

Synthetic elastic simulations

The TRM profile defined by eqs (4) and (11) assume the acoustic approximation, but they can also be applicable to an elastic medium because the elastodynamic Green's function is inversely proportional to the source-scatterer distance. To test this claim, we compute synthetic elastic seismograms and TRM profiles for a simple two-layer tunnel model with seven subwavelength scatterers.

[2] Recently, Hanafy *et al.* (2009) and Cao *et al.* (2012) used TRMs to locate trapped miners. They exploited the high-resolution and super-stacking properties of TRMs, but did not attribute this property to evanescent waves. Moreover, they only used the TRM methodology to locate trapped miners, not to characterize the distribution of scatterers in the earth.

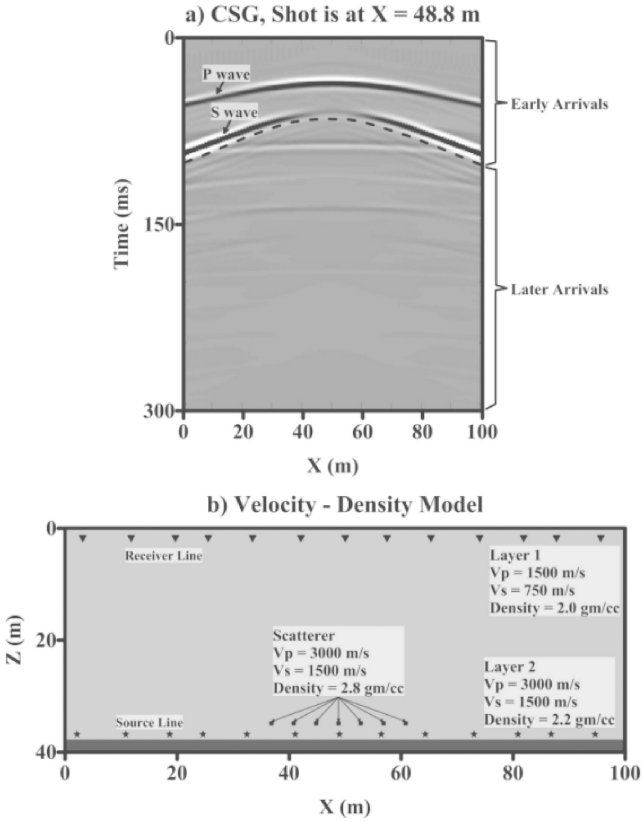

Figure 8. (a) A common shot gather (CSG) containing 181 traces with a 0.2 m trace interval and a shot location at 48.8 m. The dashed line is the boundary between early (direct-only) arrivals and later (scattered-only) arrivals. (b) Velocity model used to generate the synthetic CSGs. V_P, V_S, and density values are shown on the figure. Here, 7 scatterer points are added at a depth of 36 m from ground surface.

Fig. 8(a) shows a sample CSG at $(x, z) = (48.8, 36)$ m generated for the velocity model shown in Fig. 8(b). Here, the source is a z-component point displacement with a Ricker wavelet peaked at 100 Hz.

The TRM profile is computed according to eq. (11) by correlating the trace $d(\mathbf{g}, t|\mathbf{s}', 0)$ with the trace $d(\mathbf{g}, t|\mathbf{s}, 0)$ and summing over geophone positions at $\mathbf{g}$ to get $m(\mathbf{s}', \mathbf{s})$, the TRM profile for the actual source at $\mathbf{s}$. There are two different procedures for isolating scattered events from the direct waves.

(i) Mute the early arrivals to eliminate the direct arrivals and retain the near-field scattered arrivals. In this case, the early arrivals are defined as the energy above the dashed line in Fig. 8(a), and the remaining part defines the later scattered arrivals. Implicit in this windowing is the assumption that the near-field scattered energy is reverberating between the scatterers and the lower reflector.

Fig. 9(a) shows the TRM profile for the direct only energy where later arrivals are muted, while Fig. 9(b) shows the thinner TRM profile for the scattered only energy. This increase in resolution is due to the near-field scattering. Cross sections along (A–B) in Figs 9(a)–(b) are shown in Fig. 9(d) and represent the TRM profiles with the true source at $X = 48.8$ m. If the horizontal spatial resolution limit is defined to be the width of the main lobe at half the maximum amplitude, then the direct only resolution[3] is measured

[3] The actual wavelength is calculated $\lambda = \frac{v}{f} = \frac{1500}{100} = 15$ m.

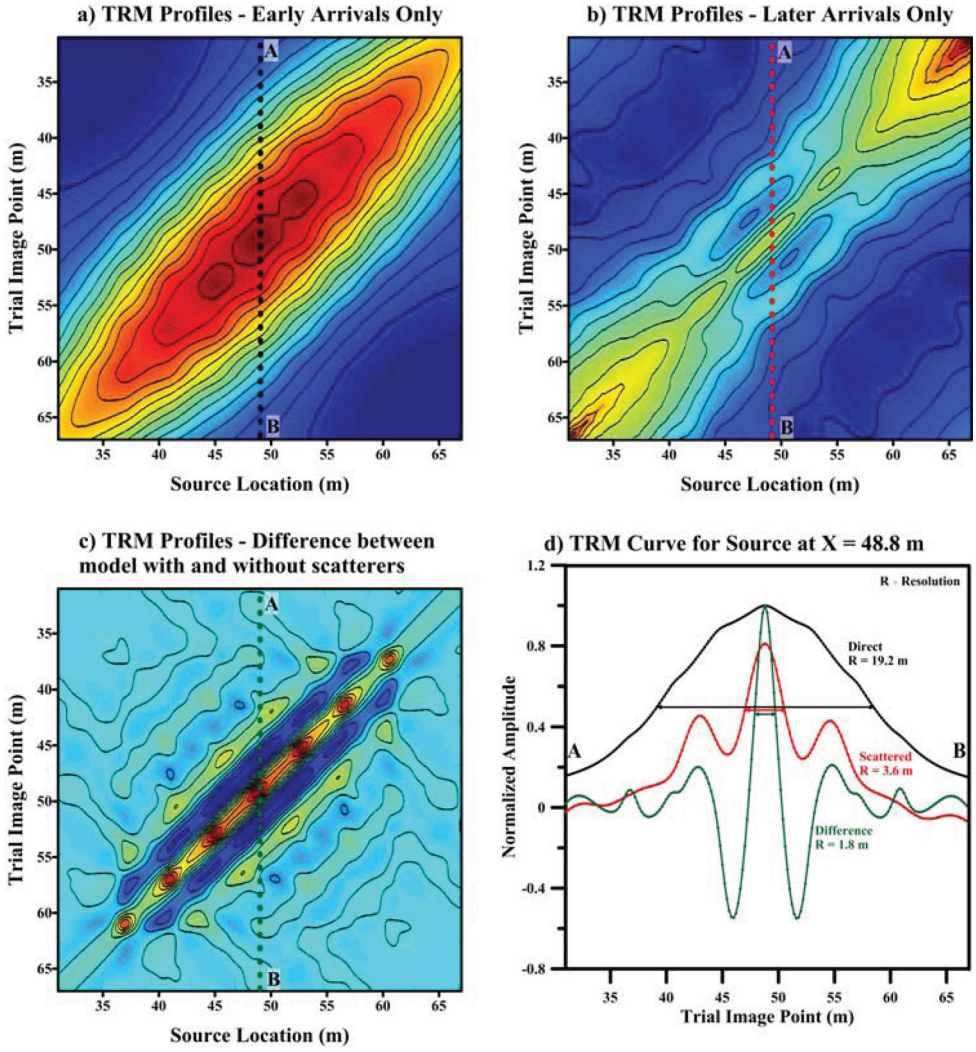

Figure 9. TRM profiles $m(\mathbf{s}', \mathbf{s})$ calculated from traces that exclusively contain (a) direct waves (b) later arrivals, and (c) scattered waves. The source location is at $\mathbf{s} = (48.8, 0)\,m$ just below the middle of the scatterers in Figs 8(b). (d) Cross sections (A–B) taken at the source location $\mathbf{s} = (48.8, 0)\,m$ for the three panels (a, b, and c).

to be $\Delta x^{direct} = 19.2m = 1.3\lambda$ and the scattered-only resolution is $\Delta x^{scatt.} = 3.6m = \frac{\lambda}{4.2}$.

(ii) Compute the CSGs for the velocity model without scatterers, compute the CSGs with scatterers, and then subtract the two data sets. This differenced CSG will be referred to as the 'differenced' Green's function. Fig. 9(c) shows the TRM profiles for the differenced Green's function. The cross-section of the TRM profile in Fig. 9(c) is plotted in Fig. 9(d) and shows a resolution of $1.8m = \frac{\lambda}{8.3}$.

The elastic simulations results confirm that TRM profiles with super-resolution can be obtained from far-field elastic scattered records. Muting the early arrivals is sufficient for obtaining super-resolution TRM profiles, but differencing seismograms is more effective.

Field data acquisition and results

The field test in the Arizona tunnel deployed 60 receivers along the free surface in Fig. 7 with a receiver interval of 0.5 m. For the source, a hammer was repeatedly struck against the side of the tunnel wall at a horizontal shot spacing of 0.5 m. At each shot location, two different files are recorded: the first one consists of the single-stacked shot gather $\mathcal{F}^{-1}[G(\mathbf{g}|\mathbf{s})]$ in eq. (2) and the second file contains the extrapolation shot gathers $\mathcal{F}^{-1}[G(\mathbf{g}|\mathbf{s}')]$ for $\mathbf{s}'\epsilon B_s$ and $\mathbf{g}\epsilon B_g$. There were 16 stacks per trace to increase the signal-to-noise ratio, and each stacked shot gather was normalized by its L_2 norm value. This last step insures that the input energy of each shot gather is about the same value. The early arrivals in the traces in Fig. 10 are first muted to give the scattered CSGs (Fig. 10). A low-pass filter with a pass range of 20–80 Hz and a stop value of 130 Hz is applied to the data, and the power spectrum of a stacked shot gather is shown at the top of Fig. 7. The Abbe horizontal resolution limit is approximately $\Delta x = \lambda/2 = 9.5$ m where the estimated minimum wavelength is $\lambda_{\min} = \frac{V_p}{\text{Frequency}} = 1470/76 = 19$ m. Here, the velocity is estimated from the collected shot gathers to be 1470 m s^{-1} and the peak frequency of the data is estimated to be 76 Hz as shown in the power spectrum at the top of Fig. 7.

Fig. 11(a) depicts the TRM profiles $m^{\text{dir}}(\mathbf{s}', \mathbf{s})$ and $m^{\frac{\text{dir}}{2}}(\mathbf{s}', \mathbf{s})$ calculated, respectively, from the early-arrival CSGs recorded in the full-aperture $m^{\frac{\text{dir}}{2}}(\mathbf{s}', \mathbf{s})$ and half-aperture[4] of traces. Here, the

[4] Eq. (11) is used to calculate the TRM profiles for the full 60-trace data and the half-aperture data where only 30 traces located along the middle of the geophone line are used.

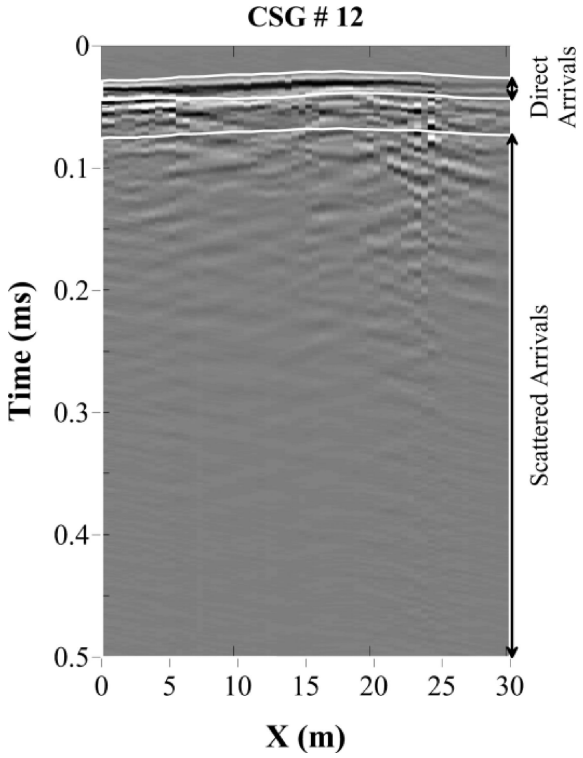

Figure 10. Recorded band-limited Green's function for a shot with the offset of 6 m along the tunnel. Direct and scattered arrivals are marked with arrows.

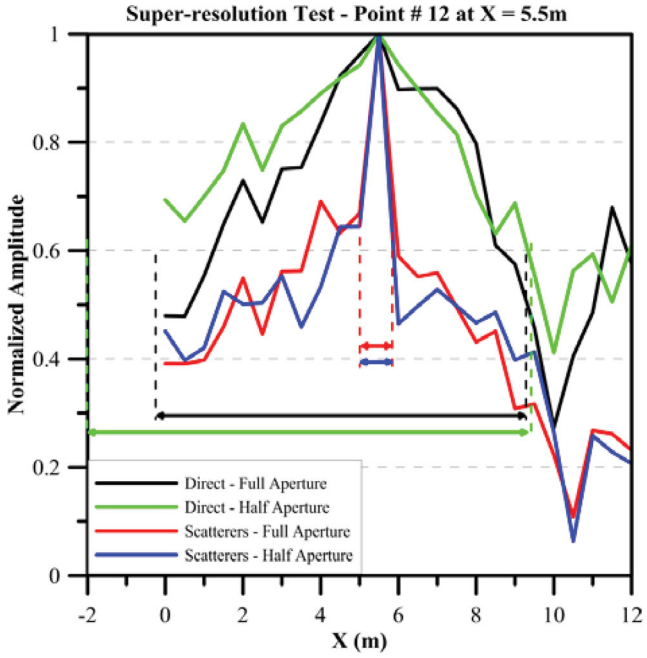

Figure 11. TRM profiles $m(\mathbf{s}', \mathbf{s})$ calculated from traces that exclusively contained either direct waves (black and green) or scattered waves (red and blue). The source location is at $\mathbf{s} = (5.5, 0)$ m where the zero depth is at the depth of the tunnel. The TRM profile is computed for source points in the mine tunnel (see bottom left-hand side picture in Fig. 7). Note the similarity of the peaked nature of these profiles to those predicted by the dashed inverse-distance function in Fig. 3.

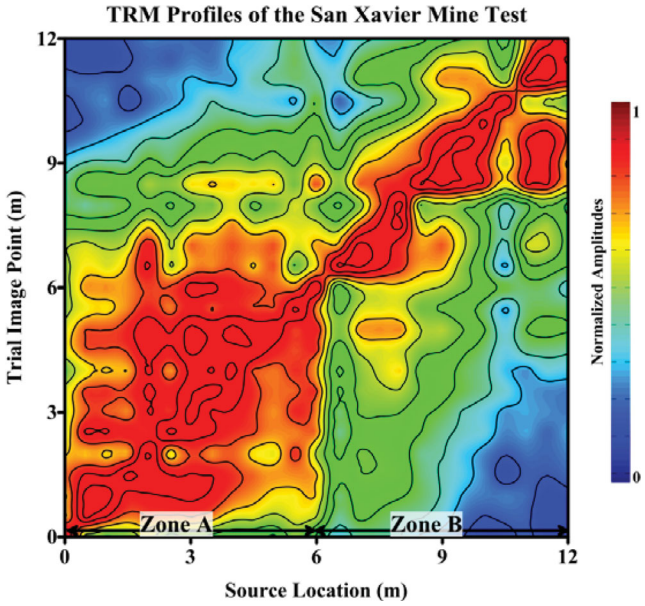

Figure 12. TRM profiles for different shot positions plotted against trial image point locations. Varying the trial image point for source locations at less than 5 m yields broad red regions around the diagonal and indicates worse spatial resolution compared to the sources at around 6.0, 8.0 and 10.5 m. The colourbar corresponds to the normalized amplitude values of the TRM profiles and the row of colours for the source location at 5.5 m is plotted in Fig. 11.

source is set to be at the location $\mathbf{s} = (5.5, 0)$ m, and the trial image points $\mathbf{s}'$ are along the tunnel where $z = 0$ at the depth of the tunnel. In contrast, $m^{\text{scatt}}(x, 0)$ and $m^{\frac{\text{scatt}}{2}}(\mathbf{s}', \mathbf{s})$ denote, respectively, the TRM profiles calculated from the scattered energy in the full- and half-aperture of traces.

If the horizontal spatial resolution limit is defined to be the main lobe width at half the maximum amplitude, then Fig. 11 shows that

(i) the horizontal spatial resolution limits of $\Delta x^{\text{scatt}}(\mathbf{x}, 0) < 1$ m and $\Delta x^{\frac{\text{scatt}}{2}}(\mathbf{x}, 0) < 1$ m are smaller than $\Delta x^{\text{dir}}(\mathbf{x}, 0) \approx 10$ m and $\Delta x^{\frac{\text{dir}}{2}}(\mathbf{x}, 0) > 11.5$ m and

(ii) if only direct arrivals are used, the horizontal resolution limit gets worse as the receiver aperture decreases.

The resolution limit for the scattered data is approximately $\lambda/19$ and is well below the Abbe limit of $\lambda_{\min}/2 = 9.5$ m.

The subwavelength resolution limit of $\Delta x^{\text{scatt}}(\mathbf{x}, 0) < 1$ m is consistent with the possibility that evanescent energy from the hammer source converts to propagating waves at nearby subwavelength scatterers, is recorded by the far-field geophones, and is digitally refocused to the source location by the TRM operation. To qualitatively estimate the distribution of these subwavelength features, Fig. 12 shows the TRM profiles at different source and trial image points. It is clear that the better resolved source point locations are at the (6, 6), (8, 8) and (10.5, 10.5) locations, which are located in the region designated as B. To the left of zone B, is Zone A characterized by broad red regions along the diagonal. This is a region of low resolution as defined by the TRM profile.

To investigate the presence of subwavelength scatterers in the tunnel, one of the authors (Hanafy) recently visited the test site and took photographs of the tunnel walls. Hanafy observed that there is a distinct separation between the two zones: Zone B in Fig. 13(b) is characterized by sharp irregular features along the tunnel walls with metre-sized inclusions of hard rock. The hardness is measured

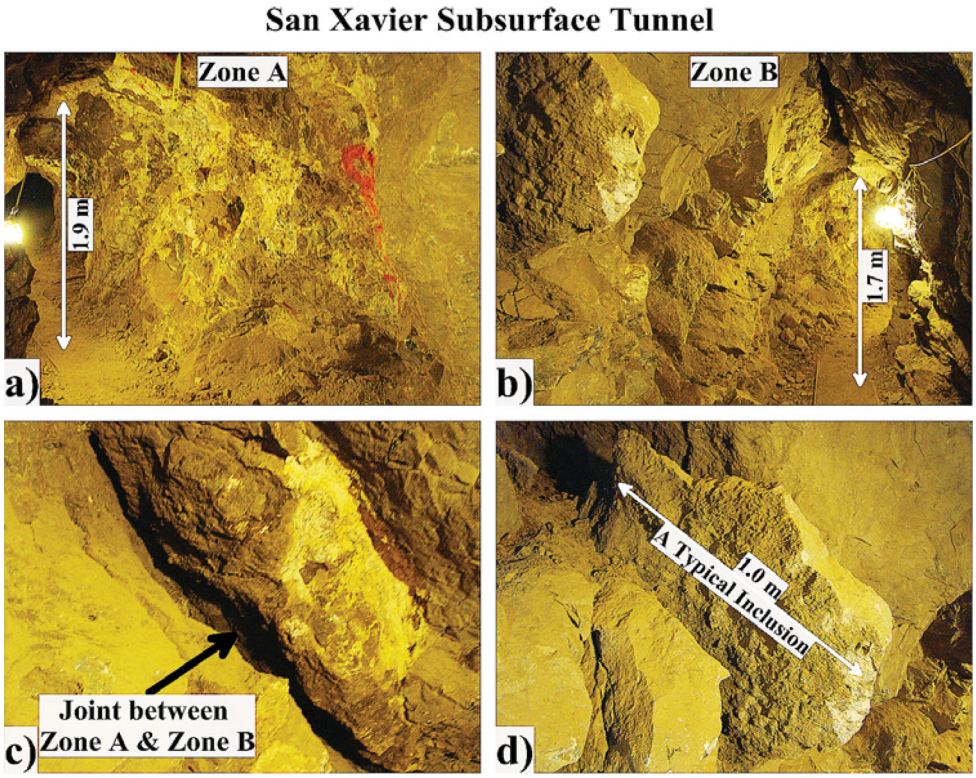

Figure 13. Photos from inside the San Xavier Mine Tunnel. (a) and (b) are along the same wall, but (a) shows mostly shows Zone A while (b) shows Zone B. The red mark on the (a) is approximately between Zones (A) and (B). (c) shows one of the joints that can be visually seen along the tunnel wall. d) is a typical inclusion about 1 m in width.

to be 6.0, surrounded by soft sediments with a hardness measured to be 2.0.

A picture of a typical inclusion is shown in Fig. 13(d), which most likely contributes to the near-field scattering. These inclusions are not visible in the Zone A portion of the tunnel (Fig. 13a). In fact, Zone A and Zone B are separated by a joint that appears to be a fault-like feature. The geologic study of this area (Sternberg *et al.* 1988) confirms that a fault and joints (Fig. 13(c)) cut through the tunnel.

Appendix C tests the sensitivity of the TRM profiles to different window widths. Results show that the indicator of superresolution, a main lobe width less than $\lambda/2$, is robust with respect to reasonable variations of window lengths. Appendix D presents the justification for normalizing each shot gather or each trace, which is necessary if the source strength is variable from one CSG to the next.

A prediction from the TRM formula is that the near-field geometrical spreading factor $\alpha(\mathbf{s}, \mathbf{o}, \mathbf{s}')$ in eq. (5) is independent of frequency, while the sinc-like function should widen with decreasing source frequency. To test this prediction, Fig. 14 shows the TRM curves for direct only and scattered only waves after applying bandpass filters of 10–40 Hz and 40–80 Hz to the input data. As predicted, the width of the filtered scattered data does not noticeably change while that of the directly arrivals widen. This supports the claim that the TRM profile is exhibiting superresolution behaviour due to scatterers in the near-field of the source.

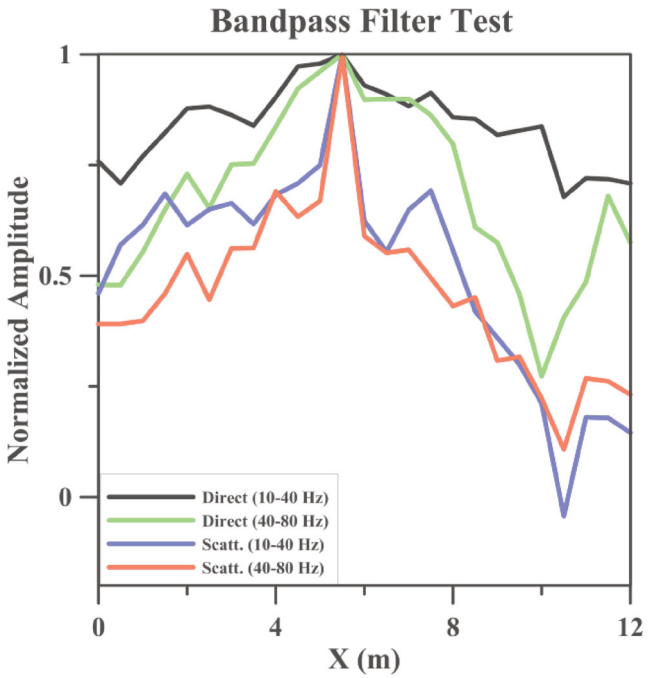

Figure 14. TRM curves for the Arizona data after bandpass filtering. Black and green curves are for the direct only waves using 10–40 Hz (black) and 40–80 Hz (green) filter, while blue and red curves are for the scattered only waves using 10–40 Hz (blue) and 40–80 Hz (red) filter.

DISCUSSION AND SUMMARY

Theoretical analysis, simulations, and a field experiment show that a TRM operation can be generated from far-field seismic data

and achieve subwavelength resolution of the scatterer's location. This assumes that there are subwavelength scatterers in the near-field of the source, the traces can be measured either in the near-field or far-field regions of the source, and scattered energy can be separated from the strong direct arrivals. Synthetic tests validate this claim, and the tests for the Arizona tunnel data support the possibility that super-resolution imaging of scatterer locations can be achieved with seismic data at frequencies in the 10–80 Hz range. For the Arizona TRM profiles, a spatial resolution of $\lambda/19$ is observed. By reciprocity, this also means that if there are subwavelength scatterers in the near-field of the geophones then the TRM operation can be applied to the reciprocal data $G(\mathbf{g}|\mathbf{s})$ to get TRM profiles at the geophones with subwavelength resolution. The source–receiver configuration for achieving this type of imaging is a line of source locations and a roughly parallel line of receiver locations that are located either in the near-field or the far-field region of the source locations. This configuration can be achieved with vertical seismic profile, surface seismic profile or crosswell field experiments.

It can be shown that the TRM operation is a special case of redatuming seismic data by interferometry (Wapenaar 2004; Schuster 2009) so that, in theory, the virtual data at the source line can be migrated to image the scatterer distribution in the near field. Thus, subwavelength imaging of the earth's reflectivity distribution in the near-field region is theoretically possible with the configuration of a scanning tunnelling macroscope.

A significant challenge is that the near-field scattered energy should be separated from the direct arrivals. There are several possible methods for achieving this goal.

(i) Mute the direct arrivals or early arrivals if there are significant near-field multiples that are visible after the first arrival. Our elastic simulations and Arizona tests required that both the *P* and *S* direct waves should be muted to isolate the scattering energy.

(ii) 4-D experiments where the seismic data recorded at different times are subtracted from one another. If there are significant subwavelength scatterer variations in the near-field then this might be visible in the subtracted records.

Separating the direct field from the near-field scattered arrivals will be the biggest challenge in achieving subwavelength resolution with a SSTM. As discussed in Appendix D, trace normalization is a possible means for accounting for the effects of sources with variable strengths.

A practical use of a SSTM might be to migrate evanescent energy in downhole data to estimate the crack intensity along the borehole; alternatively, an indirect imaging procedure is to examine the TRM profiles such as in Fig. 12. Broad smooth peaks in the TRM profiles indicate a negligible density of subwavelength cracks in the near field, while sharper peaks indicate a higher density. Similar to a spectroscope, the data can be low-pass filtered to extend the region of the near-field and assess its crack density.

The SSTM can employ surface waves as the generators of evanescent energy, and use the scattered Rayleigh waves as a high-frequency indicator of near-surface velocity variations; moreover, Stonely waves in a borehole might be used for this purpose as well. Another potential application is to use earthquake recordings, e.g. US Array, on the surface to estimate the calibration Green's functions. These calibration Green's functions might then be used to estimate the TRM profiles along the fault plane, as shown in Fig. 15. Similar to the SSTM scans shown in Fig. 12, the earthquake SSTM scans might be used to estimate the roughness of the geology near or on the fault plane. By reciprocity, the rough geology under the recording array can be assessed as well.

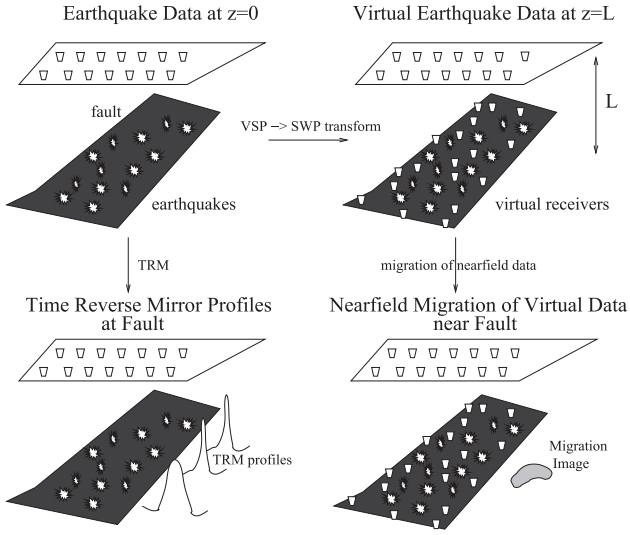

Figure 15. Earthquake data associated with a fault or a subduction zone are recorded by surface receivers. If the earthquake locations are known then the TRM profiles can be computed along the fault. Another possibility is to interferometrically redatum the traces at $z = 0$ to the fault plane itself using the data as extrapolators, which is equivalent to the VSP–SWP transform in Schuster (2009). These redatumed data can then be migrated to estimate both the near-field and far-field scatterer distributions.

REFERENCES

Bai, C., 2000. *Scanning Tunneling Microscopy and Its Applications*, Springer Verlag, New York.

Binnig, G. & Rohrer, H., 1986. Scanning tunneling microscopy, *IBM J. Res. Dev.,* **30,** 355–369.

Born, M. & Wolf, E., 1999. *Principles of Optics*, 7th edn, Cambridge University Press, Cambridge, UK.

Cao, W., Hanafy, S.M., Schuster, G.T., Zhan, G. & Boonyasiriwat, C., 2012. High-resolution and super-stacking of time reversal mirrors in locating seismic sources, *Geophys. Prospect.,* **60,** 1–17.

Claerbout, J., 1992. *Earth Soundings Analysis: Processing versus Inversion*, Blackwell Scientific Publications, Cambridge, MA.

Cragg, G. & So, P., 2000. Lateral resolution enhancement with standing evanescent waves, *Opt. Lett.,* **25,** 46–48.

de Fornel, F., 2001. Evanescent waves from newtonian optics to atomic physics, Springer-Verlag, New York, NY.

de Rosny, J. & Fink, M., 2002. Overcoming the diffraction limit in wave physics using a time-reversal mirror and a novel acoustic sink, *Phys. Rev. Lett.,* **89,** 124301-1–124301-4.

Duquet, B., Marfurt, K.J. & Dellinger, J., 2000. Kirchhoff modelling, inversion for reflectivity, and subsurface illumination, *Geophysics,* **65,** 1198–1209.

Elmore, W. & Heald, M., 1969. Physics of waves, McGraw Hill Book Company, Columbus, OH.

Fink, M., 1993. Time-reversal mirrors, *J. Phys. D: Appl. Phys,* **26,** 1333–1360.

Fink, M., 2006. Time-reversal acoustics in complex environments, *Geophysics,* **71,** SI151–SI164.

Fink, M., 2008. Time-reversal waves and super resolution, *J. Phys.: Conf. Ser.,* **124,** 1–29.

French, W., 1974. Two-dimensional and three-dimensional migration of model-experiment reflection profiles, *Geophysics,* **39,** 265–277.

Gelius, L.J., 1995. Generalized acoustic diffraction tomography, *Geophys. Prospect.,* **43,** 3–29.

Gelius, L.J. & Asgedom, E., 2011. Diffraction-limited imaging and beyond - the concept of super resolution, *Geophys. Prospect.,* **59,** 400–421.

Godin, O., 2011. Scattering of a spherical wave by a small sphere: an elementary solution, *JASA Exp. Lett.,* **130,** EL135–EL141.
Hanafy, S., Cao, W. & Schuster, G., 2009. Using super-stacking and super-resolution properties of time-reversal mirrors to locate trapped miners, *TLE,* **28,** 302–307.
Jia, H., Ke, M., Hao, R., Ye, Y., Liu, F. & Liu, Z., 2010. Subwavelength imaging by a simple planar acoustic superlens, *Appl. Phys. Lett.,* **97,** 173507-1–173507-3.
Kuhl, H. & Sacchi, M.D., 2003. Least squares wave-equation migration for avp/ava inversion, *Geophysics,* **68,** 262–273.
Lehman, S.K. & Devaney, A.J., 2003. Transmission mode time-reversal super-resolution imaging, *J. acoust. Soc. Am.,* **113,** 2742–2753.
Lerosey, G., de Rosny, J., Tourin, A. & Fink, M., 2007. Focusing beyond the diffraction limit with far-field time reversal, *Science,* **315,** 1120–1122.
Lipson, S.G., Lipson, H. & Tannhauser, D.S., 1995. *Optical physics,* 3rd edn, Cambridge University Press, Cambridge, UK.
McMechan, G.A., 1983. Migration by extrapolation of time dependent boundary values, *Geophys. Prospect.,* **31,** 413–420.
Nemeth, T., Wu, C. & Schuster, G.T., 1999. Least-squares migration of incomplete reflection data, *Geophysics,* **64,** 208–221.
Osipov, A. & Hongo, K., 1998. Green's function of an impedance wedge, *Electromagnetics,* **18,** 135–165.
Schatzberg, A. & Devaney, A.J., 1992. Super-resolution in diffraction tomography, *Inverse Probl.,* **8,** 149–164.
Schmidt, R.O., 1986. Multiple emitter location and signal parameter estimation, *IEEE Trans. Antennae Propag.,* **AP-34,** 276–280.
Schuster, G.T., 2009. *Seismic Interferometry,* Cambridge Press, Cambridge, UK.
Snieder, R., 2004. Extracting the green's function from the correlation of coda waves: a derivation based on stationary phase, *Phy. Rev. E,* **69,** 046610-1–046610-8.
Steel, M., Marks, B. & Rahmani, A., 2010. Properties of sub-diffraction limited focusing by optical phase conjugation, *Opt. Exp.,* **18,** 1487–1500.
Sternberg, B.K., Ryan, T.M., McGill, J.W. & Breitrick, M.E., 1988. The San Xavier geophysics and tunnel-detection test site: laboratory for advanced subsurface imaging (lasi), Department of Mining and Geological Engineering, University of Arizona, Tucson, AZ, **LASI-88-2,** pp. 14–37.
Stolt, R. & Benson, A., 1986. Seismic migration: theory and practice, in *Handbook of Geophysical Exploration,* Vol. 5, Geophysical Press, London, UK.
Tabib-Azar, M., Bumrerraj, S., Katz, J.L. & You, S.H., 1999. Evanescent electromagnetics: a novel, super-resolution, and non-intrusive, imaging technique for biological applications, *Biomed. Microdevices,* **2,** 73–80.
Wapenaar, K., 2004. Retrieving the elastodynamic Green's function of an arbitrary inhomogeneous medium by cross correlations, *Phys. Rev. Lett.,* **93,** 254301-1–254301-4.
Zhang, X. & Liu, Z., 2008. Superlenses to overcome the diffraction limit, *Nat. Mater.,* **7,** 435–441.

APPENDIX A: VARIOUS WIDTH MEASURES OF AN INVERSE-DISTANCE CURVE

Given the curve, which we name the inverse-distance curve in this paper,

$$\tilde{f}(x') = \frac{1}{\sqrt{\epsilon^2 + x'^2}}, \tag{A1}$$

we investigate two measures of curve width. For clarity, we shall focus on a normalized curve

$$f(u) = \frac{1}{\sqrt{1+u^2}}, \tag{A2}$$

which is related to $\tilde{f}(x')$ by $f(u) = \epsilon \tilde{f}(u\epsilon)$. The overall proportionality coefficient in front of $\tilde{f}$ does not affect the width measure of the curve; only the relationship $x' = u\epsilon$ does. Therefore, scaling the width measure associated with $f(u)$ by ϵ gives us in turn the width $\Delta x'$ associated with $\tilde{f}(x')$.

Full width at half maximum (FWHM)

The FWHM w can be derived from its definition

$$f\left(\frac{w}{2}\right) = \frac{1}{2}\max f(u) = \frac{1}{2},$$

$$\text{yielding} \quad \frac{1}{1+(\frac{w}{2})^2} = \frac{1}{4},$$

$$\text{and therefore} \quad w = 2\sqrt{3} \quad . \tag{A3}$$

So the FWHM associated with $\tilde{f}(x')$ is $2\sqrt{3}\epsilon$.

Inflection point width

An inflection point is a point on a curve where the curvature changes sign. Since the curvature of $f(u)$ can be derived as

$$f'(u) = -u(1+u^2)^{-\frac{3}{2}}, \tag{A4}$$

$$f''(u) = 3u^2(1+u^2)^{-\frac{5}{2}} - (1+u^2)^{-\frac{3}{2}}, \tag{A5}$$

setting $f''(u)$ to 0 at $u = \frac{w}{2}$ leads to

$$3\left(\frac{w}{2}\right)^2 = 1 + \left(\frac{w}{2}\right)^2,$$

$$\text{and therefore} \quad w = \sqrt{2}. \tag{A6}$$

So the inflection point width associated with $\tilde{f}(x')$ is $\sqrt{2}\epsilon$.

APPENDIX B: TRM FOR MULTIPLE SCATTERERS

The summations in eq. (11) can be split into self-interaction terms

$$m(\mathbf{s}', \mathbf{s})^{\text{self}} = \int_{-\omega_0}^{\omega_0} k|W(\omega)|^2 \sum_{B_g} \sum_{\mathbf{o}\epsilon B_o} r(\mathbf{o})^2 \; G(\mathbf{g}|\mathbf{o}) G(\mathbf{o}|\mathbf{s}) \times G(\mathbf{g}|\mathbf{o})^* G(\mathbf{o}|\mathbf{s}')^* \mathrm{d}\omega, \tag{B1}$$

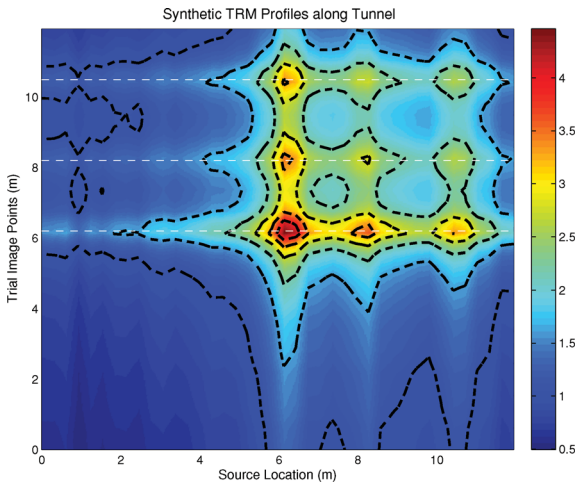

Figure B1. TRM profiles computed for the three-scatterer model described in the text. The dimensions of this model and the source frequency are similar to those for the Arizona tunnel experiment and the three dashed lines are associated with the near-field scatterers at $(x, z) = (6.2, 0.32)$, $(8.2, 0.43)$ and $(10.5, 0.36)$ m.

where $\mathbf{o}' = \mathbf{o}$ in the summations, and the remainder

$$m(\mathbf{s}', \mathbf{s})^{\text{xtalk}} = \int_{-\omega_0}^{\omega_0} k|W(\omega)|^2 \sum_{B_g} \sum_{\mathbf{o}\neq\mathbf{o}'} \sum_{\mathbf{o}'\epsilon B_o} \times r(\mathbf{o}')r(\mathbf{o})G(\mathbf{g}|\mathbf{o})G(\mathbf{o}|\mathbf{s}) \times G(\mathbf{g}|\mathbf{o}')^* G(\mathbf{o}'|\mathbf{s}')^* \mathrm{d}\omega, \quad \text{(B2)}$$

which will be termed the cross-talk term. Eq. (4) gives the analytic form of the self-interaction term for a single scatterer, and now we discuss the self- and cross-talk terms for the case of two scatterers.

For convenience, assume one geophone, $k = 1$, $W(\omega) = 1$, a single frequency, and two scatterers (one at $\mathbf{o}_1$ and the other distantly located at $\mathbf{o}_2$) with unity reflection coefficients so that the self-interaction term becomes

$$m(\mathbf{s}', \mathbf{s})^{\text{self}} = |G(\mathbf{g}|\mathbf{o}_1)|^2 G(\mathbf{o}_1|\mathbf{s})G(\mathbf{o}_1|\mathbf{s}')^* + |G(\mathbf{g}|\mathbf{o}_2)|^2 G(\mathbf{o}_2|\mathbf{s})G(\mathbf{o}_2|\mathbf{s}')^*, \quad \text{(B3)}$$

$$= \frac{e^{i\omega(\tau_{so_1}+\tau_{s'o_1})}}{|\mathbf{g}-\mathbf{o}_1|^2|\mathbf{o}_1-\mathbf{s}||\mathbf{o}_1-\mathbf{s}'|} + \frac{e^{i\omega(\tau_{so_2}+\tau_{s'o_2})}}{|\mathbf{g}-\mathbf{o}_2|^2|\mathbf{o}_2-\mathbf{s}||\mathbf{o}_2-\mathbf{s}'|}, \quad \text{(B4)}$$

and the cross-talk term B2 becomes

$$m(\mathbf{s}', \mathbf{s})^{\text{xtalk}} = G(\mathbf{g}|\mathbf{o}_1)G(\mathbf{o}_1|\mathbf{s})G(\mathbf{g}|\mathbf{o}_2)^* G(\mathbf{o}_2|\mathbf{s}')^* + G(\mathbf{g}|\mathbf{o}_2)G(\mathbf{o}_2|\mathbf{s})G(\mathbf{g}|\mathbf{o}_1)^* G(\mathbf{o}_1|\mathbf{s}')^* \quad \text{(B5)}$$

$$= \frac{e^{i\omega(\omega[\tau_{go_1}+\tau_{so_1}-\tau_{go_2}-\tau_{s'o_2}])}}{|\mathbf{o}_1-\mathbf{g}||\mathbf{o}_1-\mathbf{s}||\mathbf{o}_2-\mathbf{g}||\mathbf{o}_2-\mathbf{s}'|} + \frac{e^{i\omega(\omega[\tau_{go_2}+\tau_{so_2}-\tau_{go_1}-\tau_{s'o_1}])}}{|\mathbf{o}_2-\mathbf{g}||\mathbf{o}_2-\mathbf{s}||\mathbf{o}_1-\mathbf{g}||\mathbf{o}_1-\mathbf{s}'|}. \quad \text{(B6)}$$

The geometrical spreading factor $1/|\mathbf{o}_1 - \mathbf{s}'|$ in equations B4–B6 says that there will be rapid variations in $m(\mathbf{s}', \mathbf{s})^{\text{xtalk}}$ and $m(\mathbf{s}', \mathbf{s})^{\text{self}}$ for small changes in the trial source point location $\mathbf{s}'$ near $\mathbf{o}_1$. This is the essential property of an imaging system with super-resolution. Moreover, the $1/(|\mathbf{o}_2 - \mathbf{s}'||\mathbf{o}_1 - \mathbf{s}|)$ factor will induce both strong (strength supplied by the small denominator of $|\mathbf{o}_1 - \mathbf{s}|$ for $\mathbf{o}_1$ near $\mathbf{s}$) and rapid variations (variations supplied by $1/|\mathbf{o}_2 - \mathbf{s}'|$ for $\mathbf{o}_2$ near $\mathbf{s}'$) in $m(\mathbf{s}', \mathbf{s})^{\text{xtalk}}$ for small variations of the trial source point $\mathbf{s}'$ near the distant scatterer at $\mathbf{o}_2$. Hence, the TRM profile should, in principle, detect at subwavelength resolution the presence of the distant scatterer at $\mathbf{o}_2$ even with a far-field source at $\mathbf{s}$ and far-field receivers at $\mathbf{g}$. Indeed, far-field resolution is seen in the Fig. 6(c) profile where the source at $x = 60$ m is able to detect fine details of scatterers nearly 60 m distant.

An example of the multiple scattering response is computed for a homogeneous model (*P*-wave velocity is 1.5 km s^{-1}) with 30 embedded scatterers. This model is 12 m wide and 45 m in depth, and has the same dimensions as the Arizona tunnel experiment. Twenty-seven point scatterers with random reflection coefficients between 1 and -1 are randomly distributed from the surface to within 9 m of the tunnel. The peak frequency of the Ricker wavelet is 70 Hz to give a dominant wavelength of 21 m, so the random scatterers are mostly within the far-field region of the tunnel. Three additional scatterers at positions (6.2, 0.32), (8.2, 0.43) and (10.5, 0.36) m and characterized by reflection coefficients of 1.4, 1.0 and 1.0, respectively, are placed within the near-field region of the tunnel sources.

Generating the Born data for this three-scatterer tunnel model and using eq. (11) to compute the TRM profiles produce the TRM profiles in Fig. B1. The white dashed lines here pinpoint the three offset locations of the near-field scatterers at $X = 6.2, 8.2$ and 10.5 m. The checkerboard pattern here is consistent with the contributions from the cross-talk term.

APPENDIX C: SENSITIVITY OF TRM PROFILE TO WINDOW SIZE

This section presents results for testing the sensitivity of the TRM profile in Figs 11 and 12 to variations in window length. A desirable outcome is to show that a variety of muting windows still gives a super-resolution signature in the TRM profile, as long as the window excludes the direct arrivals of the *P*- and *S*-waves. The first test will be for the window length that only admits the early arrivals, also denoted as the 'direct waves', and the second test is that for the scattered arrivals.

Window definition

The time window for admitting direct arrivals has a length $T + 2T_o$ and takes on the unit value over a time duration of T, and linearly tapers to zero on either side of the window (Fig. C1). The value of t^b denotes the initial arrival time of the direct wave, T is the length of the time window with unit values and T_0 is the dominant period of the *P*-wave direct arrival. The taper zone on either side of the unit window is one period long.

TRM sensitivity to window width for direct arrivals

Fig. C2 shows the TRM images for traces windowed by the 'direct-wave' window with lengths from $T = T_o$ to T = $3.5T_o$. All of the

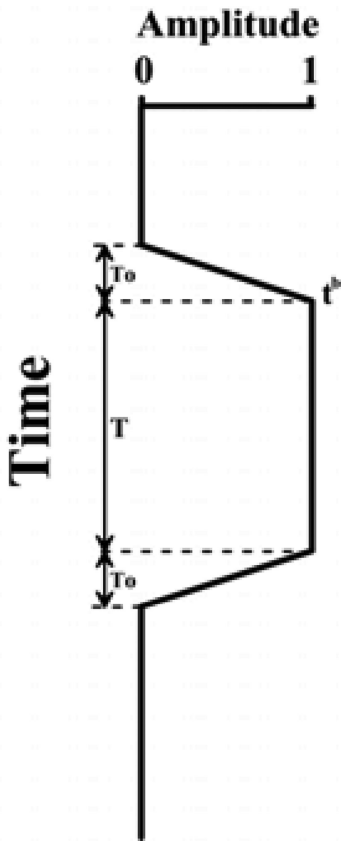

Figure C1. Pass window used to pass either direct or scattered arrivals. The total window length is $T + 2T_o$, where T is a given value and T_o is the period. t^b is the initial arrival time of the direct wave.

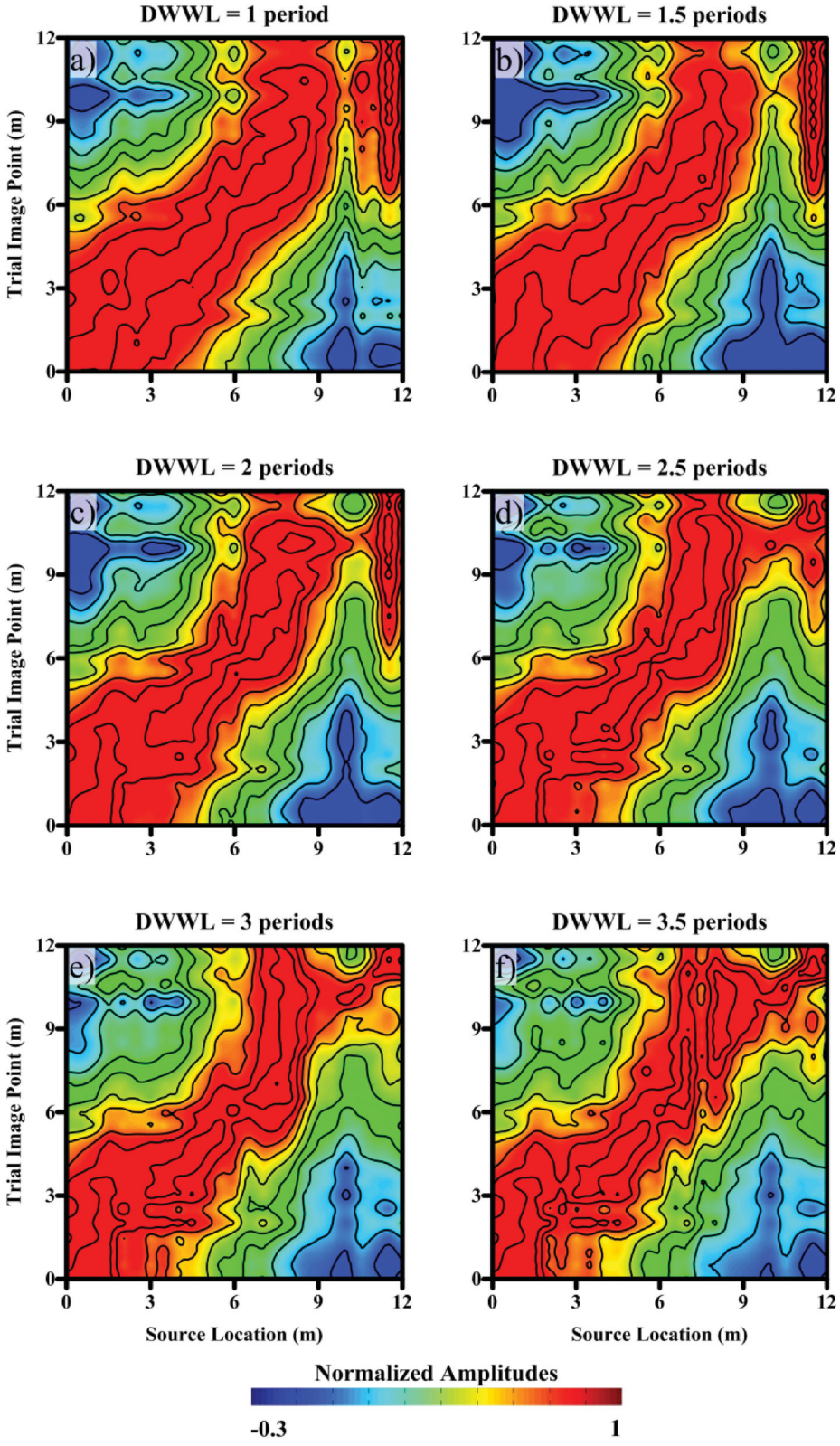

Figure C2. TRM 2-D images for various direct-wave window lengths (DWWL) of (a) 0.013 s, (b) 0.0195 s, (c) 0.026 s, (d) 0.033 s, (e) 0.039 s and (f) 0.046 s. Extending beyond the window is a tapering duration of one period $T_0 = 0.013$ s.

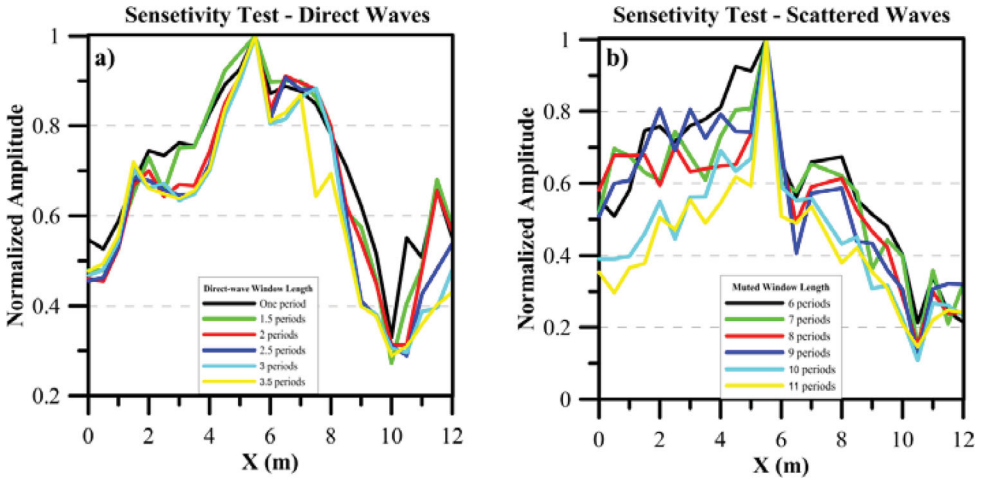

Figure C3. TRM sensitivity of the profiles for (a) direct and (b) scattered arrivals. A total of six different windows are used to show the TRM profile.

figures show broadened TRM profiles that are similar to the direct wave profile in Fig. 11, where the main lobe widths are wider than λ. This is similar to the synthetic TRM images where the large amplitudes of the non-evanescent direct waves dominates the TRM image.

Zoom views of the TRM profiles for different window lengths are shown in Fig. C3(a), and reveal that the average width of the main lobe is no larger than λ. In this example, the image point is located at 5.5 m. These results are consistent with the elastic simulations that predict that the superresolution signature will not appear if the windowed arrivals are dominated by non-evanescent direct waves.

TRM sensitivity to window width for scattered arrivals

Fig. C4 shows the TRM profiles for traces windowed by the 'scattered-wave' windows with starting times that range from 0.078 to 0.143. The ending time is 0.5 s for all of these windows, the last time of recording. All of the figures show a broadened TRM image for trial source locations from 0 to about 6 m, which suggests the absence of near-field scattering with significant energy. However, the TRM profiles with width notably less than λ/2 are found at trial source locations of 6, 8 and 10.5 m for all of the window lengths.

Zoom views of the TRM profiles for different scattered-wave window lengths are shown in Fig. C3(b), and reveal that the average width of the main lobe ranges from 0.8 to 1.6 m. This suggests the presence of strong subwavelength scatterers in the nearfield of the source location at 5.5. These results also suggest that the super-resolution signature is some what robust with respect to reasonable variations of the scattering window length.

APPENDIX D: NORMALIZATION OF TRACES AND ITS EFFECT ON THE TRM PROFILE

The practical field experiment will have a source strength that is variable for different source locations and a geophone response that might vary from one geophone to the next. To partly account for this variability, we can normalize each of the windowed traces to their maximum amplitude or we can normalize a shot gather to its L_2 norm. For the experimental data, the windowed traces include the energy after the first arrival.

The theoretical justification for normalizing the traces is the following. To account for a variable geophone response β_g, and an indeterminate source amplitude W_s, we introduce a normalization factor γ to the TRM eq. (2)

$$m(\mathbf{s}', \mathbf{s})^{\text{norm}} = k \int_{-\omega_0}^{\omega_0} \int_{-L}^{L} |W_s||W_{s'}||\beta_g|^2 \times \underbrace{G(\mathbf{g}|\mathbf{o})G(\mathbf{o}|\mathbf{s})}_{\text{scattered data}} \underbrace{G(\mathbf{g}|\mathbf{o})^* G(\mathbf{o}|\mathbf{s}')^*}_{\text{scattered data}} \gamma(\mathbf{s}, \mathbf{g})\gamma(\mathbf{s}', g)\mathrm{d}g\mathrm{d}\omega, \tag{D1}$$

where $\gamma(\mathbf{s}, \mathbf{g})$ is designed to compensate for W_s and β_g. We can assign γ be obtained by assigning it to be the scaled reciprocal of the measured amplitude of the direct arrival in the windowed trace, so that

$$\gamma(\mathbf{s}, \mathbf{g}) = \frac{1}{|W_s||\beta_g|||G(\mathbf{g}|\mathbf{s})^{\text{direct}}||}, \tag{D2}$$

where $G(\mathbf{g}|\mathbf{s})^{\text{direct}}$ is the magnitude spectrum of the direct arrival recorded at $\mathbf{g}$, the L_2 norm is assumed, and the direct arrival is assumed to be the dominant one in the windowed trace.

We can approximate the norm of the Green's function's direct wave as $||G(\mathbf{g}|\mathbf{s})^{\text{direct}}| \approx \mathbf{1}/|\mathbf{s} - \mathbf{g}|$, where $|\mathbf{s} - \mathbf{g}|$ is the source-geophone distance. Thus our compensated TRM eq. (D1) now reduces to

$$\begin{aligned} m(\mathbf{s}', \mathbf{s})^{\text{norm}} &= k \int_{-\omega_0}^{\omega_0} \int_{-L}^{L} G(\mathbf{g}|\mathbf{o})G(\mathbf{o}|\mathbf{s}) \\ &\quad \times G(\mathbf{g}|\mathbf{o})^* G(\mathbf{o}|\mathbf{s}')^* |\mathbf{s} - \mathbf{g}||\mathbf{s}' - \mathbf{g}|\mathrm{d}g\mathrm{d}\omega, \\ &= k \frac{\hat{\alpha}(\mathbf{s}, \mathbf{o}, \mathbf{s}') \sin(\omega_0[|\mathbf{o} - \mathbf{s}| - |\mathbf{o} - \mathbf{s}'|)}{[|\mathbf{o} - \mathbf{s}| - |\mathbf{o} - \mathbf{s}'|]}, \end{aligned} \tag{D3}$$

where $\hat{\alpha}(\mathbf{s}, \mathbf{o}, \mathbf{s}')$ is the compensated super-resolution factor given by

$$\hat{\alpha}(\mathbf{s}, \mathbf{o}, \mathbf{s}') = \frac{c}{|\mathbf{s} - \mathbf{o}||\mathbf{s}' - \mathbf{o}|} \int_{-L}^{L} \frac{|\mathbf{s} - \mathbf{g}||\mathbf{s}' - \mathbf{g}|}{|\mathbf{g} - \mathbf{o}|^2}\mathrm{d}g. \tag{D4}$$

For $\mathbf{s}$ and $\mathbf{s}'$ near $\mathbf{o}$, then $|\mathbf{s} - \mathbf{g}||\mathbf{s}' - \mathbf{g}| \approx |\mathbf{o} - \mathbf{g}||\mathbf{s}' - \mathbf{g}|$ is a smoothly varying factor w/r to $\mathbf{s}'$ for $\mathbf{g}$ in the farfield, and is more smooth than the sinc function in eq. (D4). Therefore the compensation in eq. (D1) is roughly equivalent to a trace-by-trace normalization factor that removes the variability of the strength of the source and the geophone response.

In practice, each stacked CSG from the Arizona field experiment was normalized by its L_2 norm. The corresponding TRM profiles roughly resembled those computed from traces where each one was normalized to a maximum amplitude of unity.

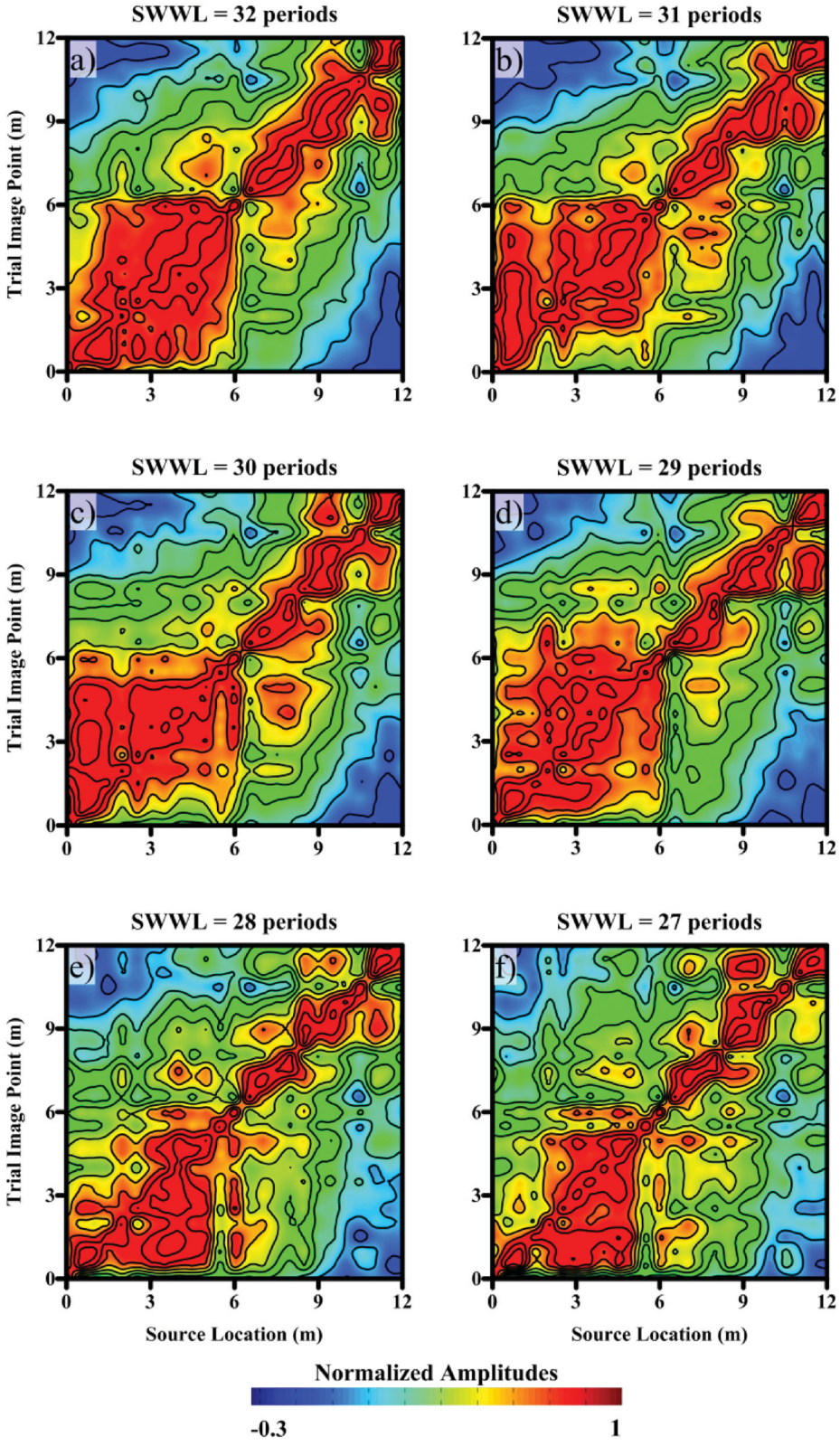

Figure C4. TRM 2-D images for various scatterer-wave window lengths (SWWL) of (a) 32 T_0, (b) 31 T_0, (c) 30 T_0, (d) 29 T_0, (e) 28 T_0, and (f) 27 T_0. The window starts at initial arrival time of the direct wave + 2 T_o.